

# Dark Matter Halo Structure in CDM Hydrodynamical Simulations

P.B. Tissera<sup>1 2</sup>, R. Domínguez-Tenreiro<sup>1</sup>

<sup>1</sup>Postal Address: Departamento de Física Teórica C-XI, Universidad Autónoma de Madrid, Cantoblanco 28049, Madrid, Spain

<sup>2</sup>Imperial College of Science, Technology and Medicine, Blackett Laboratory, Prince Consort Road, London, United Kingdom  
E-mail:rosa@astrohp.ft.uam.es

29 March 2021

## ABSTRACT

We have carried out a comparative analysis of the properties of dark matter halos in N-body and hydrodynamical simulations. We analyze their density profiles, shapes and kinematical properties with the aim of assessing the effects that hydrodynamical processes might produce on the evolution of the dark matter component. The simulations performed allow us to reproduce dark matter halos with high resolution, although the range of circular velocities is limited. We find that for halos with circular velocities of  $[150 - 200]$  km s<sup>-1</sup> at the virial radius, the presence of baryons affects the evolution of the dark matter component in the central region modifying the density profiles, shapes and velocity dispersions. We also analyze the rotation velocity curves of disk-like structures and compare them with observational results.

**Key words:** Galaxies: evolution – Galaxies: formation – Hydrodynamics – Methods: numerical

arXiv:astro-ph/9801116v1 13 Jan 1998

## 1 INTRODUCTION

The importance of understanding the formation and evolution of dark matter halos is based upon the hypothesis that they contain relevant information about cosmological parameters and the power spectrum of initial density fluctuations. Theoretical works based mainly on the second infall model, first studied by Gunn & Gott (1972), have predicted different behavior for the density profiles of dark matter halos. These models simplified the problem of the collapse of the structure by assuming spherical symmetry and purely radial motions. Fillmore & Goldreich (1984) and Bertschinger (1985) found self-similarity solutions for the secondary infall collapse. These models predict the formation of virialized objects with dark matter density profiles that are approximately isothermal. Moutarde et al. (1995) show that this result is not restricted to the fully spherically symmetric case. Hoffman & Shaham (1985) and Hoffman (1988) extended the analysis to models with different density parameters ( $\Omega$ ) and power spectra ( $P(k) \propto k^n$ ,  $-3 < n < 4$ ) concluding that density profiles of dark matter halos should steepen for larger values of  $n$  and lower  $\Omega$ . However, because of the oversimplified hypothesis assumed, these models fail to describe consistently the collapse and evolution of the structure in a hierarchical clustering scenario where the structure is formed through the collapse and aggregation of substructure. Numerical simulations are well suited to follow the hierarchical built-up of halos throughout their linear and non-linear regime (Frenk et al. 1985, 1988, Quinn et al. 1986, Efstathiou et al. 1988, Zurek et al. 1988, Dubinski & Carlberg 1991, Warren et al. 1992). During the last years there have been numerous works on the properties of dark matter halos and their implications for explaining some observational facts such as the rotation velocity curves of disk galaxies, cores of dwarf galaxies, gravitational lenses of background galaxies by galaxy clusters, etc. These techniques have resulted in a very useful tool limited mainly by numerical resolution. Several works have been carried out recently which have taken advantage of the last improvements in computational facilities and numerical techniques in order to perform high resolution numerical simulations.

In particular, several works have been dedicated to the study of dark halo density profiles in N-body numerical simulations where only the gravitational field is integrated. The most recent works by Navarro et al. (1995, hereafter NFW, 1996a,b), Cole & Lacey (1997), Tormen et al. (1997), have shown that halos in purely dynamical simulations in scale-free and Cold Dark Matter (CDM) universes in low-density, flat and open cosmologies, can be fitted by the following curve:

$$\rho(r) \propto \frac{x^{-\alpha}}{(1 + x^\beta)^\gamma} \quad (1)$$

where  $x = r/r_s$ , with a single scale radius  $r_s$ . Hernquist (1990, hereafter Hern) proposed the combination  $(\alpha, \beta, \gamma) = (1, 1, 3)$  for spherical galaxies and bulges of disk galaxies, while NFW fitted equation 1 with  $(\alpha, \beta, \gamma) = (1, 1, 2)$ . Tormen et al. (1997) analyzed the evolution of cluster halos in scale-free universes in high resolution numerical simulations, and compared the fits given by the models proposed by Hern and NFW. They found that both models described the simulated density profiles with good accuracy.

Hence, in general terms, all works seem to agree on the fact that halo density profiles in N-body simulations of scale-free and CDM models in open or flat cosmologies are curved and well described by equation 1. According to the definition proposed by NFW, this profile has two free parameters:  $c$ , the concentration parameter and  $\delta_c$ , the characteristic density. They seem to depend on the initial conditions and the mass of the halos. The characteristic density,  $\delta_c$ , is found to be proportional to the density of the universe at the time of collapse of the objects which merge to form the core halo. These authors have pointed out that dark

matter density profiles are always well-described by equation (1) and that only the values of its parameters show some dependence with the spectrum or cosmology. In particular, it has been asserted in their works that the only primordial information that dark matter profiles remember is their time of collapse.

So far all recent works have dealt with dark matter halos in purely gravitational scenarios, describing its evolution and properties as a function of mass and initial conditions. However, halos contain a fraction of baryonic matter that, although in a smaller proportion, may influence the evolution of the dark matter. There have been several attempts to address the effects of dissipation on the evolution of the dark matter component in galactic halos using different approaches to model it (Blumenthal et al. 1986, Flores et al. 1993, Flores & Primack 1994, Dubinski 1994). Blumenthal et al. (1986) used analytic models and dissipative particle collisions in N-body simulations to study the response of the dark matter halo to the presence of baryons, with the aim at understanding the origin of rotation curves of spiral galaxies. Subsequent works (Flores et al. 1993, Flores & Primack 1994) used their results to deep on the analysis of dark matter structure in halos. Dubinski (1994) analyzed the effects of dissipation on the dark matter halo by introducing an analytical potential well representing disk-like and spheroidal structures in its central region. This author found that when the baryonic component is taken into account, the overall potential well is modified in the central region leading to a change in the density profiles and shapes, in agreement with the result of Blumenthal et al. (1986). Evrard et al. (1994) analyzed the formation of galaxies in cosmological hydrodynamical simulations, finding that halos are more spherical than in purely dynamical ones.

Regarding clusters of galaxies, there have been several numerical works on the analysis of their density profiles. Observational estimates of gas and dark matter density profiles in X-ray clusters show controversial results since gas density profiles seem to be shallower ( $\rho \propto r^{-1}$ ) than those of the dark matter component, deduced by gravitational lensing techniques. Navarro et al. (1995) analyzed hydrodynamical simulations of galactic clusters and found that they could be fitted by a shallower power law:  $\rho \propto r^{-1}$ , in the central region. On the other hand, Aninos & Norman (1996) obtained a different result from high resolution simulations of galaxy clusters using a two-level grid code. They find that both gas and dark matter density profiles follow a unique power law  $\rho \propto r^{-9/4}$ . They pointed out the presence of a non-convergent gas density core even for their highest resolution run, in disagreement with Navarro et al. (1995) results. It is an uncomfortable situation that numerical studies of dark matter halos of cluster of galaxies using different techniques yield different results. Numerical resolution problems and artefacts are still unavoidable limitations, together with our ignorance of the detailed physics involved in the formation of the structure in the Universe.

From an analytical point of view, Chieze et al. (1997) and Teyssier et al. (1997) studied the adiabatic collapse of spherical symmetric perturbations of gas and dark matter. They found a segregation between gas and dark matter components. The dark matter density profiles was found to be steeper than that of the gas. According to these authors, the main effect of the joint evolution of their adiabatic purely spherical collapse is the compression of the gas core by the dark matter. But they found no changes in the dark matter density profiles. Their hypothesis of geometry and non-treatment of cooling effects may result in differences in the final properties of the gas and dark matter distributions when compared to the results of cosmological hydrodynamical simulations which also include cooling mechanisms.

Studying halos which contain both components, baryonic and dark matter, with numerical techniques is still a quite difficult task to accomplish, principally because of the high resolution required by the dissipative component, but also because of the complexity of the different processes related to the physics of baryons such as star formation, supernovae, etc.

The aim of this paper is to present a comparative analysis of galactic halos formed in simulations with and without hydrodynamical effects, and to assess any changes in the properties of the dark matter arising as a consequence of the presence of the dissipative component. Our results attempt to describe the effects of the joint evolution of the dark matter and baryons, principally in the central region of galactic-like halos. They do not intend to be conclusive because of our numerical resolution limits. We also attempt to estimate the effects of star formation history on the properties of the objects at  $z = 0$ . This paper is organized as follows. Section 2 describes the simulations. Section 3 deals with the analysis of dark matter halos and disk-like objects properties, and discusses the results. Section 4 outlines the conclusions.

## 2 SIMULATIONS

The initial distributions of positions and velocities of particles in all simulations have been set using COSMICS ( kindly provided by E. Bertschinger ). They are consistent with standard CDM cosmologies:  $\Omega = 1$ ,  $\Omega_b = 0.1$ ,  $\Lambda = 0$ ,  $b \equiv 1/\sigma_8 = 2.5$  or  $1.7$  where  $\Omega$  and  $\Omega_b$  are the cosmological and the baryonic density parameter, respectively,  $\Lambda$  is the cosmological constant and  $b$ , the bias parameter. We have adopted a Hubble constant of  $H_o = 100h \text{ kms}^{-1}\text{Mpc}^{-1}$  with  $h = 0.5$ . We studied two sets of simulations with different initial conditions (set I and II). The simulations in each set share the same initial conditions but have different hydrodynamical parameters. In all simulations we followed the evolution of 262144 particles in a periodic box of 10 Mpc. All dark, gas and star particles have the same mass,  $2.6 \times 10^8 M_\odot$ . The initial distribution of gas particles has been chosen randomly from the total particle distribution provided by COSMICS. The hydrodynamical ones (simulations I.2, I.3 and II.2) were performed using a Smooth Particle Hydrodynamical (SPH) code (see Tissera et al. 1997 for details of the SPH implementation) coupled to the high resolution adaptive particle-particle-particle-mesh code (AP3M), kindly provided by Thomas & Couchman (1992) (simulations I.2 and I.3 corresponds to simulations 6 and 3 in Tissera et al. 1997, Table I). For comparison, the same initial conditions were run taking into account only gravitational effects using the AP3M (simulations I.1 and II.1). The gravitational softening used was  $\epsilon_g = 5 \text{ kpc}$ . Unfortunately, this SPH code does not allow us to use individual time steps. The integrations were carried out with 1000 steps of  $\Delta t = 1.3 \times 10^7 \text{ yrs}$ . All simulations were integrated only gravitationally from  $z > 50$  to  $z = 10$ , and from there the SPH forces were also taken into account (Evrard et al. 1994) up to  $z = 0$ . Table I lists their main characteristics.

Hydrodynamical runs also include a star formation algorithm (Tissera et al. 1997) which allows to transform cold gas in high density regions into stars. The parameters  $\eta$  and  $\rho_{star}$  in Table I are related to the star formation scheme:  $\eta$  is the star formation efficiency and  $\rho_{star}$  is a critical density above which a cold gas particle in a convergent flow is transformed into stars. The value of  $\rho_{star}$  is estimated by requiring the cooling time of the gas cloud represented by a particle to be smaller than its dynamical time. The actual value of  $\rho_{star} \approx 7 \times 10^{-26} \text{ g/cm}^3$  used here is a minimum limit for the gas density to fulfill this requirement (Navarro & White 1993). Because of the high efficiency of the radiative cooling and the fact that no heating sources have been included, the star formation process is very efficient (a lower cutoff of  $T = 10^4 \text{ K}$  has been used for the temperatures). This leads to an early transformation of the gas into stars, and prevents the formation of disk-like structures. As a consequence, in simulations I.3 and II.2 all objects are spheroids. In simulation I.2 a smaller value of  $\eta$  was used. This allowed the gas to settle into disk-like structures, although the

star formation history of these objects was artificially delayed to low redshift. Objects in set II are dynamically more evolved than those in set I because of their higher  $\sigma_8$  value. By the same reason, objects in run II.2 have suffered from an earlier transformation of the gas into stars than those in run I.3, even if they have the same values of the  $\eta$  and  $\rho_{star}$  parameters.

The simulations performed allow us to study the properties of a set of typically resembling galactic-like objects with very different formation history and of their dark matter halos. Some of them have undergone multiple mergers (Tissera et al. 1996) while others have experienced a more quiescent evolution. So differences on the properties of halos which may arise as a result of a different evolutionary path may be assessed. However, we do not have a large range of circular velocities to study the dependence of the results on the mass.

### 3 ANALYSIS

As mentioned in the introduction, there have been several analytical and numerical works on the properties of the dark matter structure. Most of them were carried out using N-body simulations which provide the correct gravitational evolution of the dark matter. Nevertheless, several authors (eg. Blumenthal et al. 1986, Carlberg et al. 1986, Flores & Primack 1994, Dubinski 1994) have pointed out that the presence of baryonic matter might affect the evolution of the dark component by modifying the potential well in the central region, and producing a change in their shapes and density profiles. However, there have not been exhaustive studies of halos in SPH simulations. Hence, it is very interesting to carry out a comparative analysis of the properties of dark halos in purely dynamical and hydrodynamical simulations. We run sets of simulations sharing the same initial conditions but with and without hydrodynamical effects. A direct comparison between the shapes and density profiles and an assessment of the possible effects caused by dissipational mechanisms can be then carried out.

In this work, we analyzed only the more massive objects whose halos and the galaxy-like objects they host (GLOs, see below) are represented by a fairly large number of particles. We have chosen halos in hydrodynamical runs which contain more than 300 baryonic particles at their virial radius ( $r_{200}$ ). Hence we describe the properties of the dark halos of 20 galaxy-like objects in hydrodynamical simulations and 12 in purely gravitational ones. Halos have been identified at their virial radius according to the discussion of White & Frenk (1991). The virial radius is the radius where the density contrast of the fluctuation reaches a value of  $\delta\rho/\rho \approx 200$ . In the hydrodynamical case, baryons are included so the virial radius corresponds to that of the total mass distribution (baryons and dark matter). In simulations of set II, we have discarded some objects that belong to groups and therefore, share a common dark halo. However, in set I we keep halo 7 because it hosts only two main baryonic clumps which assembled at very low redshift. The halo mass center is defined by an iterative method which searches for the mass center of concentric spheres of decreasing radius. The process is halted when the number of particles in the sphere equals a certain fixed number. This algorithm has been proved to converge quickly. The baryonic clumps within  $r_{200}$  of a halo are isolated using a friends-of-friends algorithm with a linking length of the order of 10% the mean particle separation. We will refer to them as galaxy-like objects. It has to be noted that the center of mass of the halos may not coincide with the center of mass of the principal galaxy it hosts. This is due to the presence of satellites within its virial radius. The difference between both mass centres may be of order of 3 – 6 kpc. Table II summarizes the principal characteristics of halos and the GLOs they host (spheroids (S), disks (D) and pairs (SP or DP)).

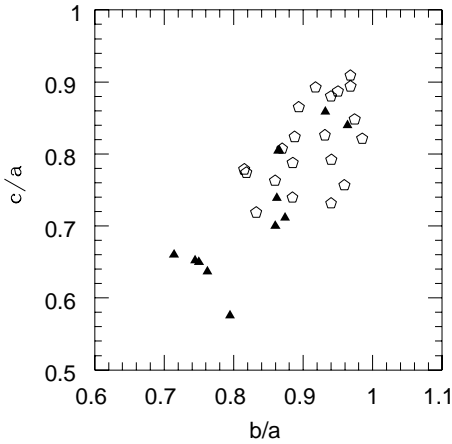


Figure 1.

### 3.1 Shapes

In order to analyze the shapes of dark matter halos, we follow a procedure based upon the discussion presented by Curir et al. (1993, and references therein). Basically, we calculated a sequence of concentric ellipsoids containing fractions of the total mass of the objects. We identify inside this region a sequence of 10 concentric ellipsoids containing fractions of 10 % to 100 % of the total mass:

$$r = \left[ x^2 + \frac{y^2}{(b/a)^2} + \frac{z^2}{(c/a)^2} \right]^{1/2} \quad (2)$$

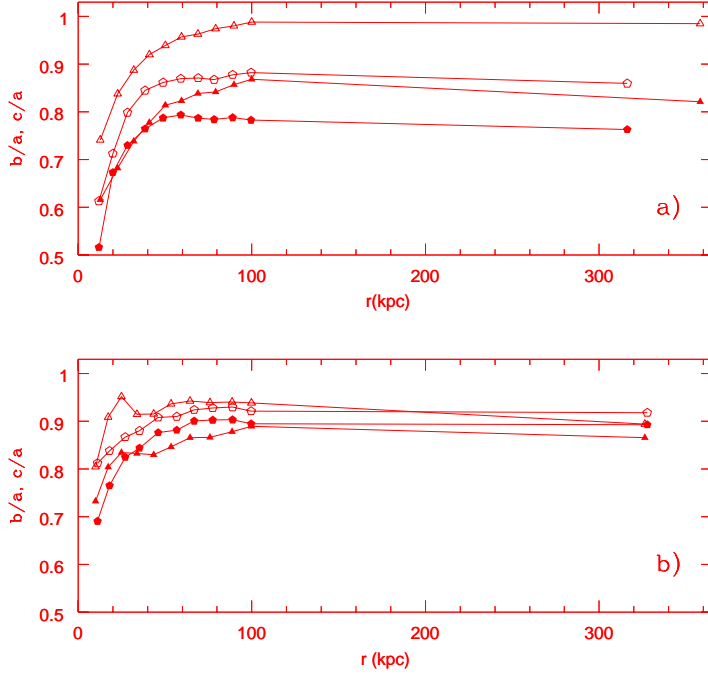
The semiaxes of the triaxial ellipsoids ( $a > b > c$ ) are calculated iteratively :

$$\frac{b}{a} = \left( \frac{I_{22}}{I_{11}} \right)^{1/2}, \quad \frac{c}{a} = \left( \frac{I_{33}}{I_{11}} \right)^{1/2} \quad (3)$$

where  $I_{11} > I_{22} > I_{33}$  are the eigenvalues of the tensor of inertia ( $I_{jk} = \sum_i \frac{x_i^j x_i^k}{[r_i]^2}$ ). In order to determine  $a, b$  and  $c$ , an iterative cycle is required starting with  $\frac{b}{a} = \frac{c}{a} = 1$ . The eigenvalues are calculated for these first axial ratios, and then a new set of semiaxes is estimated which constitutes the input of the next iteration. The procedure is repeated until the axial ratios  $\frac{b}{a}$  and  $\frac{c}{a}$  have a percentage change of less than  $10^{-3}$ . The axial ratios are estimated for each of the ten ellipsoids.

Fig. 1 shows the ratios  $b/a$  and  $c/a$  for all halos in simulations I.2, I.3 and II.2 (open pentagons), and their dissipationless counterparts in simulation I.1 and II.1 (solid triangles) at the virial radius. As already discussed by several authors (eg. Dubinski 1994, Evrard et al. 1994), halos formed in purely gravitational simulations tend to be more prolate. Halos in simulation I.1 and II.1 have on average  $\langle b/a \rangle = 0.83$ ,  $\langle c/a \rangle = 0.78$  at  $r_{200}$ . The same halos, but in the hydrodynamical runs, have modified their shapes and are more spherical, and they show, on average, a minor flattness  $\langle b/a \rangle \approx 0.91$ ,  $\langle c/a \rangle \approx 0.81$ .

Another estimator of shapes is the parameter  $T = (a^2 - b^2)/(a^2 - c^2)$ . For a purely prolate object  $T = 1$ , while for a purely oblate,  $T = 0$ . The average value of  $T$  for I.1 and II.1 is  $\langle T \rangle = 0.63$ , while for their hydrodynamical counterparts,  $\langle T \rangle = 0.51$ . This result shows how the shapes of halos change from prolate to more oblate ones when the dissipational properties of the gas are taken into account.


**Figure 2.**

An inspection of the different ellipsoids defined according to equation 2 shows the dependence of shapes on radius. From  $r = 100$  kpc to  $r_{200}$  the shapes are quite stable. So we calculated the axis for a sequence of 10 ellipsoids containing fractions from 10% to 100% of the dark mass within  $r = 100$  kpc. In Fig. 2a, we can see the ratios  $b/a$  (open) and  $c/a$  (solid) for halos containing a disk-like (pentagons) and a spheroidal (triangles) structure (both objects are in simulation I.2). All objects tend to be more prolate in the central region becoming more oblate-like with increasing radius. If we compare the distribution of shapes of the halos with disks and spheroids, we find that halos with disks tend to be slightly more prolate in the central regions

In Fig. 2b, we compare the shapes of a halo containing a disk in I.2 (pentagons) and its counterpart in I.3, where all objects are spheroids (triangles). A weak trend to more oblate structures is found in halos hosting spheroids. In this case, the ratio  $c/a$  (solid triangles) is smaller than  $c/a$  for halos with disks (solid pentagons), except in the central region where the relation is the inverse. Although our sample is quite small to draw a conclusion from it, the general trend agrees with Dubinski's work who found that adding a spheroidal potential well at the center of a halo produced a stronger effect on its shape than placing a disk-like potential.

### 3.2 Kinematical Properties

We calculated the velocity dispersion tensor in spherical coordinates in the reference system of each halo:

$$\sigma_k^2(r_i) = \frac{1}{N+1} \sum_{j=i-N/2}^{i+N/2} [V_k(r_j) - \bar{V}_k(r_i)]^2 \quad (4)$$

where

$$\bar{V}_k(r_i) = \frac{1}{N+1} \sum_{j=i-N/2}^{i+N/2} V_k(r_j) \quad (5)$$

and where  $V_k$  (with  $k = r, \theta, \phi$ ) are the velocity components in spherical coordinates,  $N + 1$  is the number of particles in a bin (we have taken  $N = 200$ ) and  $r_i$  is the position of the  $i^{\text{th}}$  dark matter particle relative to the center of mass. All velocity dispersions have been calculated at particle positions by first sorting the particles according to their distance to the center of mass of the halo and, then, binning in concentric spherical shells of a fixed  $N + 1$  number of particles, where each  $i^{\text{th}}$  particle is placed at the middle point of the bin.

In isotropic systems the velocity dispersion in each coordinate should be  $3^{-1/2}$  of the total dispersion ( $\sigma$ ). We found that  $\sigma_r/\sigma$  is slightly greater than  $\sigma_\theta/\sigma$  and  $\sigma_\phi/\sigma$ . This fact is reflected in the anisotropy parameter  $\beta_{dark} = 1 - \frac{\sigma_\theta^2}{\sigma_r^2}$ . Fig. 3a shows  $\beta_{dark}$  for halo 4 in I.2 and halo 2 in I.3 (heavy lines), and their gravitational counterparts (light lines) as examples. All halos are nearly isotropic at the center but show an increasing anisotropy as a function of the distance to its mass center, reaching an average maximum of  $\beta_{dark} \approx 0.3 - 0.5$ . So the outer regions of the halos are more dominated by radial dispersions. There are no significant systematic differences among the values of  $\beta_{dark}$  of halos in different simulations. However, small differences may be covered up by the noise originated by the discreteness in the number of particles. In order to have an estimation of the strength of the signal over this noise, we measured  $\beta_{dark}$  for a simulated dark matter halo of 10000 particles consistent with a King model (King 1966). The rms dispersion found was  $\Delta rms \approx 0.11$ . Hence, the anisotropy of the velocity distribution estimated for the simulated halos can be regarded as a real signal. On the other hand, the statistical significant features individualized in the graphics of Fig.3a can be matched with the presence of satellites or substructures within  $r_{200}$ . The positions of these substructures change within simulations mainly due to modifications in the collapse times of satellites originated by hydrodynamical effects (Navarro et al. 1995).

By contrast, a difference is found among their total velocity dispersions. Fig. 3b shows the velocity dispersions of halos 1, 2, 3, 4 in simulations I.1 (light lines) and I.2 (heavy lines). It can be seen from this figure that  $\sigma$  of halos in hydrodynamical simulations increases by a percentage of approximately 59% between  $r = 100$  kpc and  $r = 10$  kpc. In the purely gravitational simulations, however, the percentage is significantly smaller, 10%, remaining practically flat over the whole range of radii. This effect is clearly related to the presence of a baryonic core in the central region of the halo which modifies the overall potential well.

We have also compared the velocity dispersion profiles of halos in simulations I.2 and I.3. As mentioned above, these simulations differ from each other only on their star formation efficiency which has led to the formation of spheroidal objects in I.3, while, conversely, I.2 has also disk-like structures. We found that the velocity dispersion of a halo hosting a disk and the same halo with a spheroid in its central region, does not show any significant difference in our simulations.

### 3.3 Halo Density Profiles

We calculated the density profiles of dark matter halos for simulations in sets I and II. The density profiles have been defined by binning the particles in spherical shells centred at the halo mass center. We work with weighted profiles using shells containing a fixed number of particles (30 or 50). We also estimated the density profiles by binning in the logarithm of the radius. Both procedures yield the same results. We have preferred to carry out the analysis



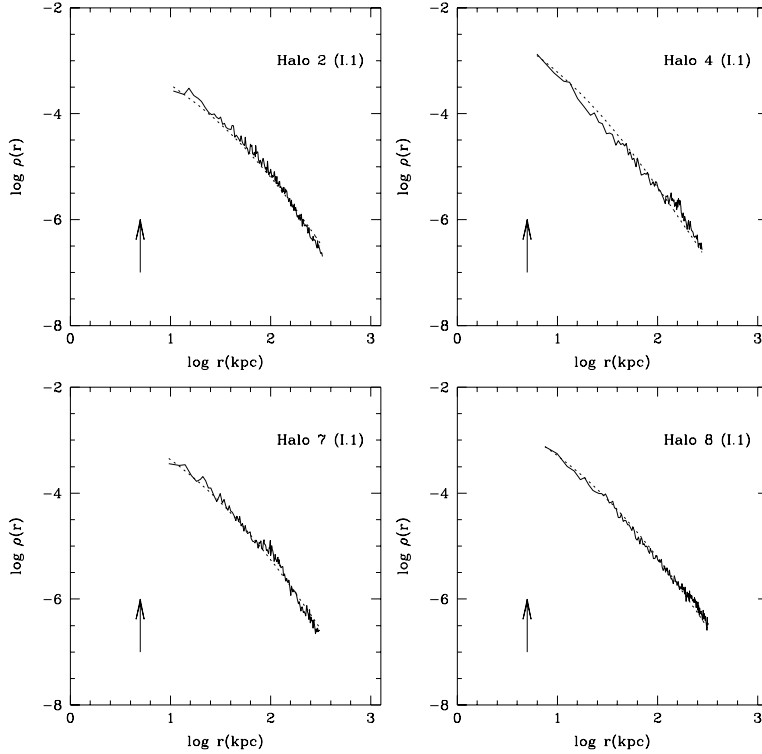


Figure 3.

using the weighted profiles since the other one gives too much weight to the central region where the resolution is lower ( $r < 2\epsilon_g$ ).

We first analyzed the density profiles of dark matter halos in purely dynamical runs (I.1 and II.1). We found that these halos fit the NFW profile remarkably well. So their density profiles steep up as  $r^{-1}$  in the central region as predicted by NFW and Hern. We also observed that more massive halos are less concentrated than smaller ones. The concentration parameters  $c_{NFW}$  found for our halos are consistent with the values published by NFW (Table II). Fig. 4 shows four halo density profiles in a N-body run (I.1) and the corresponding fitting using NFW model (solid and dashed lines respectively).

Following the same procedure, we calculated the density profiles of dark matter halos in the hydrodynamical runs (simulations I.2 , I.3 and II.2). These halos show some differences as can be seen in Fig. 5, where the density profiles of halos 1 and 3 in simulations I.1 and I.2 have been plotted. The solid line represents the density profiles in the hydrodynamical run and the dashed lines the corresponding profiles in the purely dynamical one. Since the simulations share the same initial conditions for both, velocities and positions, and gravitational parameters (softening, force errors), the differences found among the density profiles may be directly related with hydrodynamical effects.

These figures show clearly how the density changes because of the presence of a baryonic core at the center of the halo. In Fig. 6, we plot the density profiles of halos 1, 2, 3, 4 in simulation I.2 (solid lines). We also include the best fit obtained using NFW profiles (dot-long dashed lines). The slope of the density profiles of these halos is steeper in the central

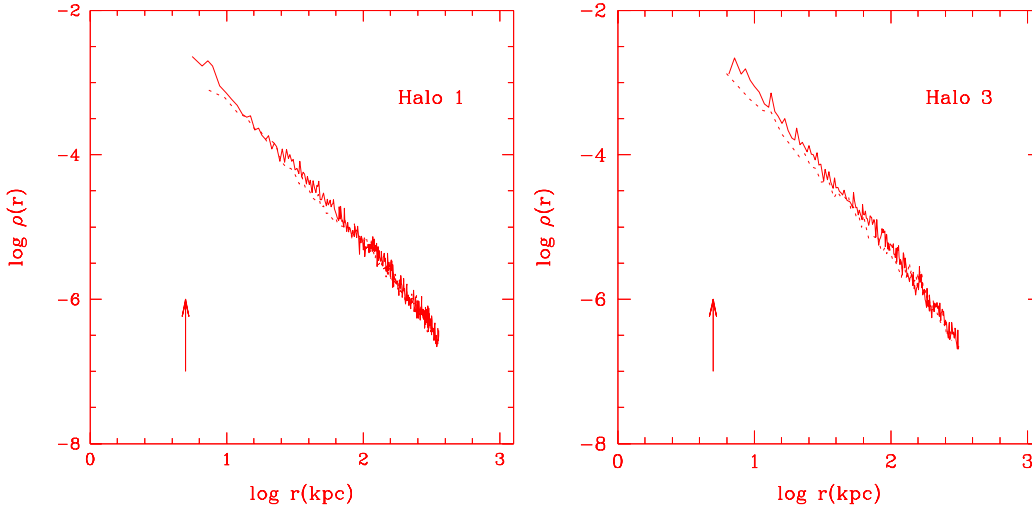


Figure 4.

region, so the profiles defined by Navarro et al. (1995) are too curved to fit them<sup>\*</sup>. Our profiles seem to follow a simple power law over a larger range of radius than NFW profiles. The radius at which NFW profiles depart from our simulated profiles correlates with the radius of the galaxy-like object in the halo (we define  $r_b$  as the radius at which the baryonic and dark matter density profiles intersect each other. See section 3.3.1 for details). It has to be stressed that the dynamical resolution of our halos is comparable with NFW objects for the same range of circular velocities.

We use a standard algorithm to fit to these profiles a power law in the central region ( $\rho \propto r^\alpha$ ), looking for the value of  $\alpha$  that gives the best fit. Values ranging from -1.9 to -2 were found. Hence, we decided to keep the functional form defined by equation 1, but increasing the slope of the power law for small radius:

$$\rho(r) = \frac{A_c}{(r/r_s)^2(r/r_s + 1)^2} \quad (6)$$

where  $r_s = r_{200}/c_{TD}$  and the  $c_{TD}$  is the parameter defined by NFW as the concentration<sup>†</sup>. The parameter  $A_c$  is determined by requiring that the total density contrast at the virial radius equals  $200\rho_{crit}$ . For equation (6) we obtain:

$$A_c = \frac{\rho_{dark}}{3} c_{TD}^2 (1 + c_{TD}) \quad (7)$$

where  $\rho_{dark} = M_{dark}^{200}/v_{200}$ . The mean dark matter density at  $r_{200}$ ,  $\rho_{dark}$ , can be rewritten

<sup>\*</sup> The parameter  $\delta_c$  has been redefined for consistency in a similar way as in equation 6:  $\delta_c = \frac{c^3 M_{200}^{dark} \rho_{crit}^{-1}}{3v_{200}[\ln(1+c)-c/(1+c)]}$ , where  $M_{200}^{dark}$  is the dark matter within the virial radius and  $v_{200}$  is the volume defined by the virial radius

<sup>†</sup> This is, in fact, the functional form studied by Jaffe (1983) for spherical systems.

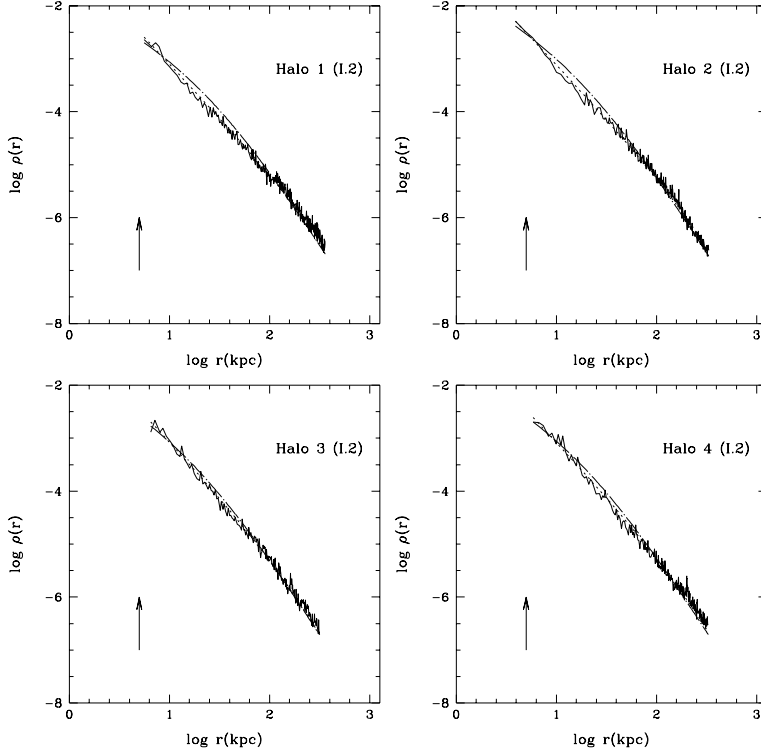


Figure 5.

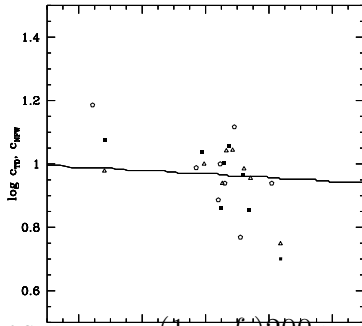


Figure 6.

as  $\rho_{\text{dark}} = \frac{2}{3} (1 - f_b) \rho_{\text{crit}}$  where  $f_b$  is the fraction of baryons within  $r_{200}$ . This fraction is almost constant ( $\approx \Omega_b$ ) for all halos. The profile defined by equation (6) was fitted to all halos in the hydrodynamical simulations. In Fig. 6, we also plot the best fit for halos 1, 2, 3, and 4 using equation (6) (dotted lines). The parameters obtained are summarized in Table II. As can be seen from this table,  $c_{TD}$  values are smaller than  $c_{NFW}$  ones, implying larger values of  $r_s$  for halos in hydrodynamical runs. This can be understood taking into account that, in equation (6),  $r_s$  is the radius that sets the transition from  $\rho(r) \propto r^{-4}$  for larger radius to  $\rho(r) \propto r^{-2}$  for the intermediate region, while, in NFW,  $r_s$  delimitates the change in the slope from  $\rho(r) \propto r^{-3}$  to  $\rho(r) \propto r^{-1}$  in the central region.

Fig. 7 shows the correlation found between the logarithm of  $c_{TD}$  and  $M_{200}$  for the density profiles of halos in simulations I.1 (open pentagons), I.2 (solid squares) and I.3 (open triangles). The zero point of the relation for objects in I.2 and I.3 has been redefined by adding an arbitrary constant to the logarithm of  $c_{TD}$  in order to place them in the same region of the diagram as the logarithm of  $c_{NFW}$ . This figure shows that larger masses are

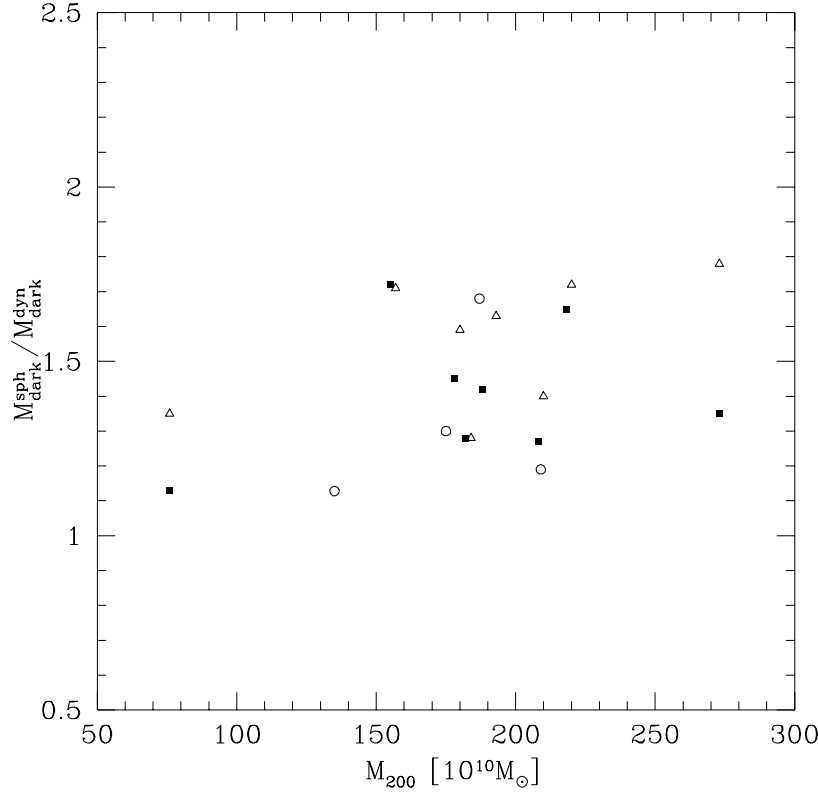


Figure 7.

less concentrated, as pointed out by NFW for purely dynamical simulations. We also include the theoretical predictions for  $c_{NFW}$  from the collapse time assuming NFW density profiles (we used an algorithm kindly provided by these authors to estimate the collapse time of the halos). With this figure we intend only to compare the slope of the relations for the hydrodynamical and N-body runs. The slope of the correlation for halos in I.2 and I.3 seems to be consistent with the relation obtained from the purely dynamical simulations. Note, however, that the range of masses is small to get a general trend. We did not find a difference between halos hosting a disk or a spheroid. In any case, a large sample with higher hydrodynamical resolution and dynamical range is needed to have a more robust statistical signal.

We measured the ratio  $\frac{M_{dark}^{sph}}{M_{dark}^{dyn}}$  where  $M_{dark}^{sph}$  and  $M_{dark}^{dyn}$  are the dark matter masses for halos in the hydrodynamical and the purely dynamical cases within a radius of  $r = 30$  kpc, respectively. This ratio roughly estimates the pulling of the dark matter by the baryons (Blumenthal et al. 1986). In Fig. 8 we plot it versus  $M_{200}$ . As can be seen from this figure, it does not seem to correlate with mass. The fact that it does not show a correlation with the mass in the range of velocities we are working with, indicates that all halos in our sample seem to have been squeezed by approximately the same factor due to the presence of the baryons. If it is valid, then the slope of the correlation between the concentration parameters and  $M_{200}$  could be still determined by the collapse time of the object.

At this point, it is worth noting that, in the absence of heating sources (like supernovae energy injection) the baryonic matter overcools at high redshifts leading to the formation of highly concentrated objects (see for example Navarro & Steinmetz 1996). This effect may also affect the evolution of the dark matter in the central region of the halos by increasing artificially the concentration of particles. In spite of this fact, as discussed by other authors,

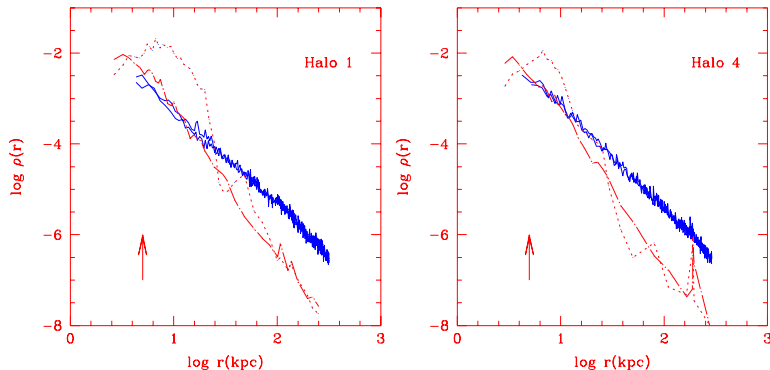


Figure 8.

the presence of baryons does change the matter distribution and this is clearly observed in our simulations, although the effect may be not as strong as measured here. We will come back to this point in the next sections.

### 3.3.1 Baryonic Density Profiles

We construct the density profiles for the baryonic matter belonging to each halo listed in Table II by following the same procedure described in section 3.3 for the dark matter component. The density profiles of baryons are not as accurate as the dark matter ones since the number of particles used to solve the gaseous component is lower than the one used for the dark matter.

As an illustration of the general behaviour of the baryonic component, Fig. 9 shows the density profiles for baryons and dark matter for two halos in set I. These two profiles intersect each other at a certain radius,  $r_b$ , which can be taken as a measure of the physical size of the central galaxy-like object. The same is true for the other GLOs listed in Table II. The  $r_b$  values range from 14 kpc to 30 kpc, but they are difficult to be properly determined because of the noisy character of the baryonic density profiles.

Note first that the baryonic density profiles (dot-long dashed and dotted lines) are steeper than the dark matter ones (solid lines). The slope for radius greater than  $r_b$  is  $\rho_{bar}(r) \propto r^{-3}$ . Secondly, that the baryonic dark matter profiles in the central region depend on the star formation parameters used. In simulation I.2 (dotted lines), baryons seem to have collapsed more dramatically than in I.3. In this last run (dot-long dashed lines), the baryonic density profiles follow the dark matter for  $r < r_b$ , changing its slope to  $\rho_{bar}(r) \propto r^{-2}$ . This is consistent with the fact that the gas has been more efficiently transformed into stars and that stars behave in a similar fashion as dark matter particles since they are only affected by gravitational forces. On the other hand, in I.2 the higher concentration of baryons in the central region is the consequence of a higher efficiency in the cooling of the gas particles. Hence, the history of star formation is relevant to the final distribution of baryons in the central region. However, from our simulations we cannot detect a clear change in the dark matter density profiles (solid lines) as a result of the difference in the baryonic distributions.

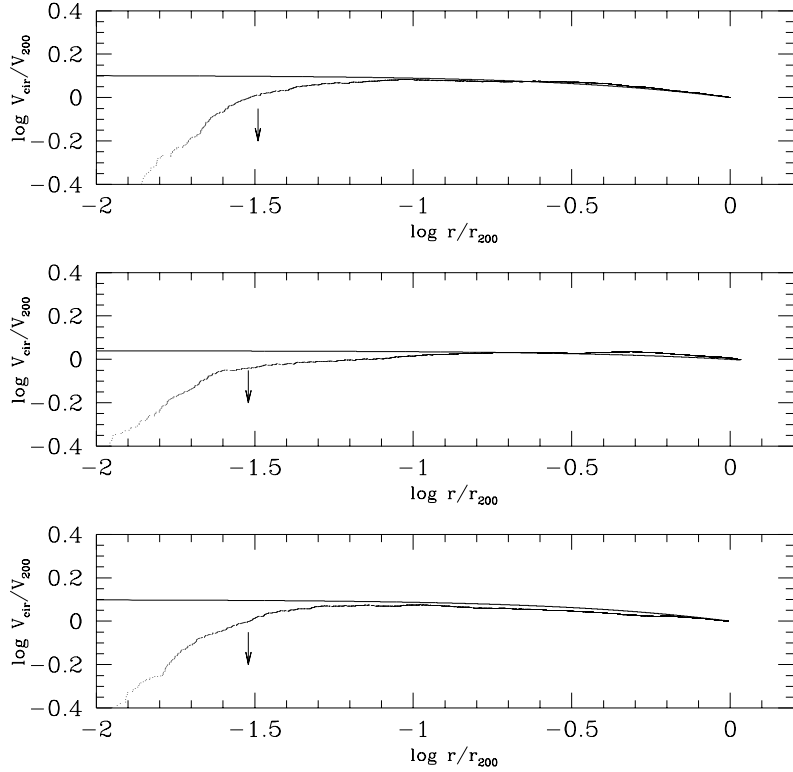


Figure 9.

### 3.3.2 Circular Velocities

The first consequence of the difference between dark matter density profiles of halos in hydrodynamical simulations and purely gravitational ones is that the maximum of the circular velocity curves ( $V_{cir}^2(r) = GM(r)/r$ ) of these halos translates towards smaller radii. In simulation I.1,  $r_{dark}^{max}$  is around 50 – 80 kpc. Whilst in simulations I.2 and I.3,  $r_{dark}^{max}$  is found at approximately 20 – 30 kpc .

According to equation (6), the circular velocity curve of dark matter halos is given by :

$$V_{cir}(r) = \frac{V_{200}(1 + c_{TD})^{1/2}}{(1 + \frac{r}{r_s})^{1/2}} \quad (8)$$

where  $V_{200}$  is the circular velocity of the dark matter at the virial radius. This curve agrees with the circular velocity for an isothermal sphere for inner radii, but decreases as  $r^{-0.5}$  for larger ones. As an example, Fig. 10 shows  $V_{cir}(r)$  for halos 1, 2 and 4 in simulation I.2 and the fitting using equation (8). As can be seen from this figure, the analytical fit is very good except for small radius where the effects of numerical resolution on the integrated mass is noticeable (the arrows point out  $r = 2\epsilon_g$ ). Our numerical resolution does not allow us to properly described the density profiles of either, the dark matter or the baryons, within 5 kpc. Numerical simulations with much higher resolution would be needed in order to assess the slope of distribution of dark matter in the very central region.

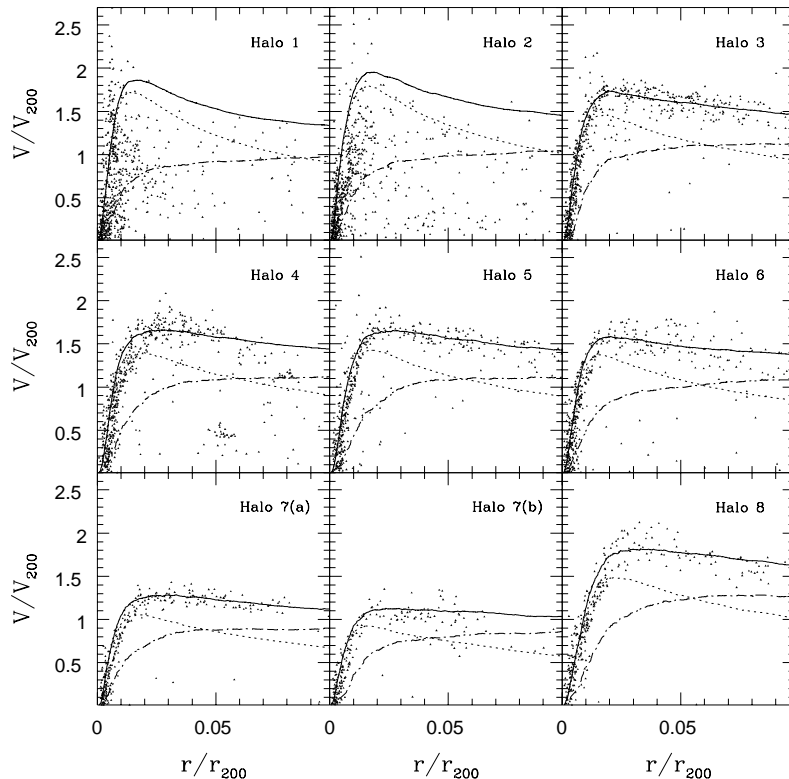


Figure 10.

### 3.4 Rotational Properties

The problem of understanding the rotation velocity curves of spiral galaxies has been analyzed in several works from observational (Persic et al. 1996 (PSS) and references therein) and theoretical points of view (Blumenthal et al. 1986, Flores et al. 1993). In this paper, we study the rotational properties of disk-like objects formed in cosmological hydrodynamical simulations and whose halos were previously analyzed in section 3.3.

We construct the rotation velocity distributions of the disk-like structures formed in halos in simulation I.2 by calculating the tangential velocity component of the baryonic particles belonging to the disks, in a cylindric reference system defined by the direction of the angular momentum of the disk with origin at its center of mass. Fig. 11 shows the rotation velocity distributions for 7 disk-like objects (solid triangles; recall that halo 7 hosts a pair of disks). Two extra objects have been included which are not purely disk-like structures but spheroids and are more massive than any of the disks shown (halos 1 and 2). We also include in this figure the equilibrium circular values of the velocities for the total mass (solid lines). We adopted the softened Plummer potential (Evrard et al. 1994):

$$V_{cir}^2(r) = \frac{GM(r)r^2}{(r^2 + \epsilon_g^2)^{3/2}} \quad (9)$$

As can be seen from this figure, baryonic particles in disk-like objects are in coherent rotation with tangential velocities which show small dispersions about the  $V_{cir}(r)$  curves, reflecting the fact that they are in rotational supported equilibrium within the potential well of the dark halos. For the spheroids, the tangential velocities appear to be disordered,

showing that no disk coherent rotation exists. We also plotted the circular velocities of the dark (dot-dashed lines) and baryonic (dotted lines) components separately.

In simulation I.3 no disks have been formed, so we look at the circular velocity of baryons and dark matter of the objects as an indicator of mass distribution and for comparison, in order to assess differences mainly due to a different star formation history (Fig. 12). We find interesting differences when equivalent galaxy-like objects in simulations I.2 and I.3 are compared. First of all, as already mentioned, the percentage of remanent gas in run I.3 is much lower and there are no clear disk-like structures. The gas distributions are spheroidal structures with  $\langle c/a \rangle \approx 0.5$ . The two baryonic objects which are spheroids in simulation I.2 are also spheroids in run I.3. The rest of the objects has a tenuous gas disk. In any case, the baryon fraction at a given  $r/r_{200}$  in the inner regions is lower for GLOs in simulation I.3, as can be seen from Figs. 11 and 12.



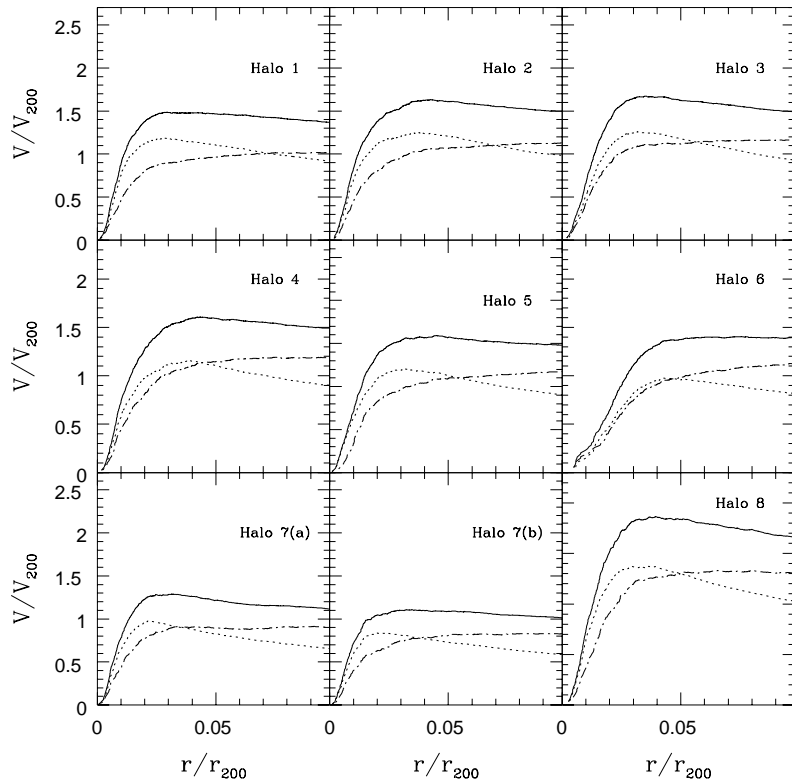


Figure 11.

### 3.5 Baryonic and Dark Matter Distributions in the Inner Regions

An interesting observation coming out from Figs. 11 and 12 is that the baryonic and dark matter distributions cross each other at a certain radius (crossing radius,  $r_{cross}$ ). This radius is the limit which divides the baryonic dominated region from the dark matter one. Hence, the rotation curves are dominated by the baryonic matter for  $r < r_{cross}$ , while the dark component is preponderant for larger radius. The values of  $r_{cross}$  for GLOs in hydrodynamical runs are given in Table II. Recall that the GLOs shown in Figs. 11 and 12 are exactly the same, but with different star formation histories (Table I)

The first question to be addressed is whether the halos and the GLOs they host present a self-similar mass distribution, that is, whether the baryon density profiles are self-similar when normalized to the parameters  $r_s$  and  $A_c$  that determine the self-similar character of the dark matter profiles (see section 3.3). A positive answer would mean that the baryon distribution is mainly determined, at any scale, by the dynamics of the dark matter halos, and would imply that  $r_{cross}/r_s$  is the same for all the GLOs belonging to a given run. This is not the case, as can be deduced from Table II, suggesting that, at small scales, the baryon distributions are linked to some other physical processes.

In order to study these distributions, we have analyzed the possible correlations of  $r_{cross}/r_{200}$  (the fraction of the virial volume dominated by baryons) with a global halo dynamical parameter ( $M_{200}$  or  $V_{200}$ ), on one hand, and with local measures of the baryon distribution at the central region of the GLOs, on the other. Crossing radii normalized to the virial radii have been used instead of the crossing radii themselves to properly assess any effect that could arise with independence on the halo size.

In Fig. 13a we plot  $V_{200}$  versus  $r_{cross}/r_{200}$ , finding no clear correlation between these pa-

rameters. However, halos with similar virial velocities are found to have different  $r_{cross}/r_{200}$ . This fact implies that their inner regions are dominated by baryons at a different extent.

In Fig. 13b we plot the maximum of the circular velocity curve,  $V_{cir}^{max}$  (see equation 9), versus  $r_{cross}/r_{200}$  for GLOs shown in Figs. 11 and 12. This graphic shows a correlation for objects in simulations I.2 and I.3. The meaning of this correlation is the following. On one hand,  $V_{cir}^{max}$  is a measure of the total mass within a sphere of radius  $r_{bar}^{max}$  (that, as seen from Figs. 11 and 12, is mainly made of baryons) and of the compactness of its distribution. On the other hand,  $r_{cross}/r_{200}$  increases when the fraction of baryons to dark matter in the inner regions of the rescaled version of the GLOs increases. So the correlation merely expresses the fact that an increase in the baryon fraction in the inner regions of the GLOs (normalized to their total size) is linked to an increase in the total (baryon plus dark) mass inside  $r_{bar}^{max}$ , and/or the compactness of its distribution. A more detailed analysis of this very inner region of the GLOs is not possible to carry out since they lie within the dynamical resolution of the simulations.

Note from Figs. 11 and 12 and Table II that  $r_{cross}/r_{200}$  is smaller for GLOs in simulation I.3 than for their counterparts in run I.2, and even smaller for objects in run II.2. In Fig. 13(a,b) these differences are also noticeable. We think that these differences in the values of the crossing radii are due to the fact that the gas has been transformed into stars more efficiently and from earlier times in I.3, and, when star particles are formed, they are instantaneously treated as collisionless. Hence, the collapse of the cold gas towards the centre of the object might not have been that effective in this simulation. This same effect can also explain the small  $r_{cross}/r_{200}$  values in GLOs belonging to run II.2, where the star formation process has started even at higher redshifts.

A related question is whether or not the fraction of the total baryonic mass inside the virial radii of the halos that is accreted at their centre depends on the virial mass of the halos. To clarify this point, we have also plotted the ratio  $M_{bar}^{cross}/M_{bar}^{200}$  versus  $M_{200}$  (Fig. 14). As can be seen from this figure, no correlation has been found for objects belonging to the same run, or, at least, it seems that it would be too weak to be detected with our sample. This figure shows that the fraction of baryons in the central regions of the GLOs grows from run II.2 to I.2. This effect is equivalent to the differences found for  $r_{cross}/r_{200}$  among objects belonging to different runs, and can be explained taking into account the differences in their star formation histories as discussed above.

We now try to understand how the results just described are originated. Let us first consider how numerical resolution can affect the infall of baryonic matter. According to Navarro and Steinmetz (1996), gaseous disk-like objects resolved with a few hundred of particles have their gas density artificially smoothed and the accretion and collapse of the disk is delayed. However, the effects measured by these authors could be larger than the ones present in our simulations since, in their low resolution experiments, the authors diminished the resolution of both, the dark matter and baryons. Taking into account the results of Steinmetz and White (1997), this is the scenario that produces the larger numerical artifacts, since also the potential wells of the halos are poorly represented. In our simulations, the potential wells onto where the baryons collapse are described with similar resolution to the high resolution runs of Navarro and Steinmetz (1996). On the other hand, the objects chosen from our simulations to be analyzed are resolved with several hundred of gas particles, varying by a factor of 2 (Table II). So, larger objects are slightly better resolved than smaller ones. Nevertheless, because of the similar number of gas particles used, we would tend to think that with our hydrodynamical resolution limits, all objects are likely to be affected at the same level. Note also that Fig. 14 shows no correlation for this sample, implying no dependence of the baryonic infall within the crossing radius on the halo virial mass. Secondly,

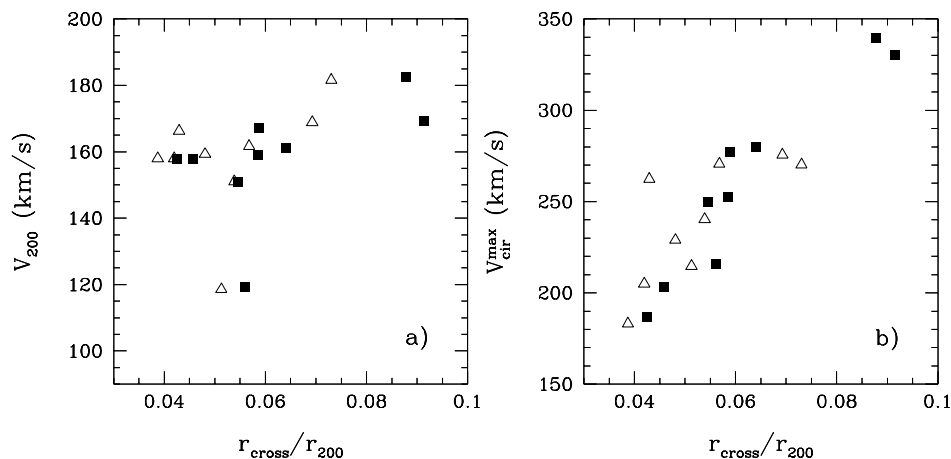


Figure 12.

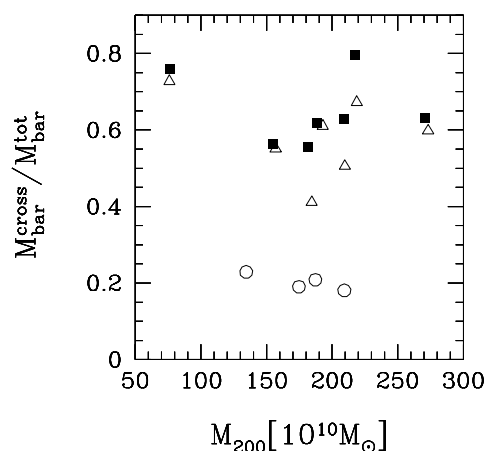


Figure 13.

we consider the possible effects of overcooling. Taking into account the relation between the cooling time and the dynamical time of a collapsing object, the cooling process are more effective at higher redshifts, producing the early collapse of baryons onto the potential wells of the first halos. Hence, overcooling effects would lead to a correlation we do not find, since smaller baryonic objects would be more affected than larger ones which have a later collapse, and, consequently, would have a higher fraction of baryons at their centres.

So, we need to invoke different mechanisms to explain Figs. 13(a,b) and 14. Let us now consider the characteristic evolutionary path a GLO goes over in a hierachical clustering scenario, where they are built up through mergers of smaller baryonic units composed of gas and stars. These mergers take place within dark matter halos, that have previously suffered their own mergers and virialized, and are characterized by parameters such as the structure, mass, relative orientation, orbital angular momentum and orbital energy of the two baryonic clumps that are to merge (Navarro et al. 1995). These parameters vary in each case, and for each merger process, they vary along the time in a complicated manner. So, each GLO

has its own merger tree of baryonic clumps, that, in addition, may determine in part its star formation history (Tissera et al. 1996). These trees may be (and in most cases they are) different for different GLOs, even if the global dynamical characteristics of the halos that host them are similar. More precisely, some authors (Hernquist 1989, Barnes & Hernquist 1991, 1996) have suggested that during a merger process of baryonic units, a gas inflow is expected to be drawn towards the central region as a consequence of a transference of angular momentum from the gas component to the collisionless matter. In particular, Barnes & Hernquist (1991) studied the dynamics of gas in a merger using a N-body/hydrodynamical code without star formation. They found that the gas component in the inner half of each disk loses most of its angular momentum and falls into a compact cloud at the center of the galaxy. Even if our simulations are not directly comparable to these results, mainly because star formation results in bulge-like baryonic cores that could slow down the gas inflow rates (Mihos & Hernquist 1994), they suggest that mergers of baryonic clumps can be highly efficient in driving gas towards the center of galactic objects. This suggests the possible existence of a correlation between the number and the characteristics of mergers suffered by a baryonic object and its crossing radius, and, moreover, the absence of correlation between this quantity and the virial mass of the halos. So mergers might be considered as an effective mechanism to redistribute the gas component within the radius of a galactic object leading to more concentrated objects. Hence, the combined history of star formation and mergers seems to be relevant to determine the distribution of baryons in the inner regions of halos and, therefore, the properties of the rotation curves of GLOs. Phenomenologically, this translates into the need for additional parameter(s), other than a halo scale and a halo characteristic density, to describe these rotation curves, in accordance with the findings of PSS. These authors claim that an extra parameter (the galaxy luminosity) is needed to characterize the shape of the *normalized* rotation curves of the galaxy sample they have studied.

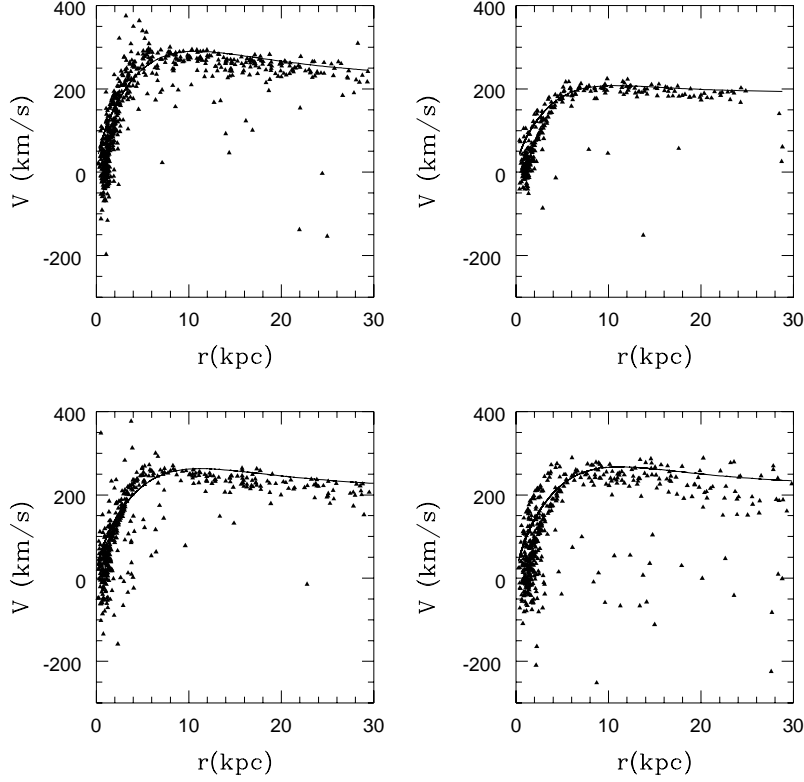


Figure 14.

### 3.5.1 Comparison to Observations

PSS point out that spiral galaxies in their sample with  $V_{rot} > 200 \text{ km s}^{-1}$  have decreasing rotation curves, while less massive galaxies have almost flat rotation curves. These authors derived from observations of rotation velocities and luminosities that the ratio between dark matter and baryonic matter inside the optical radius (defined as the radius that encloses 83% of the luminous mass of the disk), was an inversely increasing function of velocity. Thus, the inner part of high luminosity spirals seems to be dominated by luminous matter, while, conversely, low luminosity objects are dominated by dark matter. Bigger disks in our simulations (in the sense that they are more massive at radii smaller than  $r_{cross}$ ) tend to have larger crossing radii, in agreement with the results of PSS. Hence, the kinematics of massive disks seems to be strongly determined by the luminous mass.

We attempt to fit the circular velocity curve of the disks shown in Fig. 11 using the functional relation found by PSS (Universal Rotation Curve, URC). Their observational sample is composed by late-type spirals with almost no bulge contribution. So, the baryonic mass distribution is modelled as an exponential disk. These authors assumed a simple density profile for the dark matter with a core. The resulting rotation curve is obtained as a sum of the disk and halo contribution whose parameters are adjusted using observational data. They obtain:

$$V_{URC}(R/R_{opt}) = V(R_{opt}) \left[ (0.72 + 0.44 \log \frac{L}{L_*}) \frac{1.97x^{1.22}}{(x^2 + 0.78^2)^{1.43}} + 1.6 \exp[-0.4(L/L_*)] \frac{x^2}{x^2 + 1.5^2 (\frac{L}{L_*})^{0.4}} \right]^{1/2}$$

where  $x = R/R_{opt}$ , and  $R_{opt}$ ,  $V_{opt}$  and  $L$  are the optical radius, the velocity at the optical radius and the luminosity in the B-band.

Eventhough the hypotheses assumed by these authors do not agree with the properties of the objects identified in our simulations, namely, they have a bulge contribution and the dark matter density profiles are singular in the centre, we have been able to fit the URC proposed by PSS to the circular velocity curves of our disks (see Fig. 15). The *shape* of the simulated disk-like objects is not in disagreement with the *shape* of the URC as shown in this figure for four disks. However, for a simulated disk, the  $L$  parameter can be also obtained from the ratio of the baryonic to the total mass (baryons plus dark matter) contributions to the circular velocities at  $R_{opt}$  (see PSS for details). The values of this parameter obtained by these two methods are inconsistent. That is, the shapes of the rotation curves can be fitted for a given set of the free parameters, but the values of these parameters are meaningless, implying that this agreement does not result from underlying physical processes. This is not surprising, given the incompatibility of the hypotheses in PSS and the characteristics of the simulated disks we have obtained. A detailed discussion of this issue is delayed to a forthcoming paper.

#### 4 SUMMARY

We have carried out a comparative study of galactic objects in N-body and hydrodynamical simulations paying special attention to the analysis of the properties of the dark matter in galactic halos in both kinds of scenarios. Our main aim was to assess any differences in the evolution of the dark matter caused by the dissipative characteristic of baryons. This kind of analysis presents several difficulties mainly due to numerical resolution limitations and the simplicity of the model used. Nevertheless, we think the results obtained clearly show the importance of studying the joint evolution of both components in galactic-scale systems.

We arrive at the following results:

1- In agreement with other authors we find that density profiles of dark matter halos in N-body simulations can be fitted by the analytical profile suggested by NFW or Hern.

2- The consistent treatment of the joint evolution of dark matter and baryons allows to detect a difference in the evolution of the dark component when compared to purely dynamical models:

a- The shapes of dark matter halos change from prolate to more oblate structures when baryons are included. The dark matter halos in hydrodynamical simulations are more prolate in inner region becoming more spherical at larger radius. A slight difference in shapes was measured when comparing halos which host a disk or a spheroidal baryonic object. Nevertheless, a statistical analysis over a larger sample should be carried out to confirm these results.

b- The anisotropy parameter  $\beta_{dark}$  shows that dark matter halos are nearly isotropic in the central region becoming more dominated by radial dispersions at larger radius.

c- The total velocity dispersion of dark matter component is affected by the presence of baryons. A stronger increase of  $\sigma$  is measured in the central region of all halos in hydrodynamical simulations than in their purely gravitational counterparts. We did not detect any dependence of  $\sigma$  on the shape of the main baryonic clump at the center of the halo.

d- The density profiles of dark matter halos in SPH simulations are fitted by neither NFW nor Hern profiles. A steeper power law is required in the central region. Instead we fit all density profiles of dark matter halos in SPH simulations with the curve defined by equation 1, but with the combination of power:  $(\alpha, \beta, \gamma) = (2, 1, 2)$ . Hence, the profiles agree

with the behavior of an isothermal sphere for a larger interval of radius. The ratio  $\frac{M_{dark}^{sph}}{M_{dark}^{dyn}}$  indicates that approximately all our halos have been squeezed by the same factor, and that this factor does not depend on their mass.

3- We estimate the density profiles of baryons finding a segregate behaviour with respect to the dark matter. Baryons are more centrally concentrated. We also observe that the slope of the baryonic density profiles depends on the star formation parameters. Those halos formed in simulation I.2 where a delayed star formation was forced, are more baryonic concentrated; whilst in the rest of the halos, the baryonic density profiles followed the behavior of dark matter density profiles in the central region. However, we found no differences among their dark matter density profiles.

4- We analyze the circular velocity curves of the dark matter, baryons and the rotation velocity curves for disk-like objects identified in SPH simulations. We find no correlation between the  $r_{cross}/r_{200}$  and the virial mass of the halos. On the other hand, no systematic differences are found in the infall of baryons within  $r_{cross}$  among the halos analyzed. However, we found a clear correlation between the maximum of the circular velocity curves and  $r_{cross}/r_{200}$ . Hence, this correlation seems to be originated in a different distribution of baryons within the central regions. One possible mechanism which could produce this effect are mergers with substructure. The values of  $r_{cross}/r_{200}$  seem also to depend on the history of star formation. If a large fraction of gas is transformed into stars at early times, the objects are less dominated by baryons in the central region since they cannot collapse so efficiently.

5- We have been able to fit the URC proposed by PSS to the simulated rotation velocity curves. We find a set of URC parameters which allows to match to the *shapes* of the curves. However, the luminosities of simulated disks can also be found by considering the contributions of baryons and dark matter to these curves. The two methods produce inconsistent results, mainly due to the high concentration of baryons in the inner regions of GLOs. So, the fits do not carry any physical information.

To sum up, the joint gravitational evolution of dark matter and baryons in a hierarchical clustering model, together with physical processes such as radiative cooling, star formation, supernovae, etc, may be all non-negligible interrelated ingredients to take into account when trying to fully understand how disk galaxies formed, and in particular, to explain their rotation curves. In this paper, we analyzed the effects of introducing hydrodynamics and star formation on the properties of galactic-like structures in CDM simulations. There are several aspects such as the star formation mechanism and processes related to it, dynamical resolution and range, which would require to be improved in future works. Furthermore, overcooling effects are unavoidable without including heating sources like supernova energy ejection. The properties of the central region of all our halos in the SPH runs may be affected by them. Therefore, the models studied here and their outcomes are first results from where underpin more sophisticated ones. These facts will be discussed in future works where we will analyze more complex models.

## ACKNOWLEDGEMENTS

We thank the referee of this paper for a careful reading and useful comments and suggestions. P. Tissera was supported by the Ministerio de Educación y Ciencia (Spain) through a fellowship for foreign scientists. P. Tissera would like to thank Prof. Rowan-Robinson and the Astrophysics group at ICSTM for their hospitality and support, and to Prof. Efstathiou

and the Astrophysics group at the University of Oxford for providing the computational support required to perform this paper.



## REFERENCES

- Aninos, P. , Norman, M. L., 1996, *ApJ*, 459, 12  
 Barnes J., Hernquist, 1996, *ApJ*, 471, 115  
 Barnes J., Hernquist, 1991, *ApJ*, 370, L65  
 Bertschinger, E., 1985, *ApJS*, 58, 39  
 Blumenthal G. R., Faber S. M., Flores R. A., Primack J. P., 1986 *ApJ*, 301, 27  
 Carlberg R. G., Lake G., Norman C. A., 1986, *ApJ*, 300, L1  
 Chieze, J., Teyssier, R., Alimi, J.-M, 1997, *ApJ*. Submitted  
 Cole S., Lacey C. G., 1996, *MNRAS*, 281, 716  
 Curir A., Diafero A., De Felice F., 1993, *ApJ*, 412, 70  
 Dubinski J., Carlberg R., 1991, *ApJ*, 378, 496  
 Dubinski, J., 1994, *ApJ*, 431, 617  
 Efstathiou, G. P., Frenk, C. S., White S.D.M., Davis M., 1988, *MNRAS*, 235, 715  
 Evrard, A.E., Summers, F. J., Davis, M. 1994, *ApJ*, 422, 11  
 Fillmore, J.A., Goldreich, P., 1984, *ApJ*, 281,1  
 Flores R. A., Primack J. R., 1994, *ApJ*, 427, L1  
 Flores, R. A., Primack J. R., Blumenthal G. R., Faber S. M., 1993, *ApJ*, 412, 443  
 Frenk, C. S., White, S. D. M., Efstathiou, G. P., Davis, M., 1985, *Nature*, 317, 595  
 Frenk, C. S., White, S. D. M., Davis, M., Efstathiou, G. P., 1988, *ApJ*, 327, 507  
 Gunn, J., Gott, J. R., 1972, *ApJ*, 209, 1  
 Hernquist, L., 1989 , *Nature*, Vol 340, 687  
 Hernquist, L., 1990, *ApJ*, 356, 359 (Hern)  
 Hoffman, Y., 1988, *ApJ*, 328, 489  
 Hoffman, Y., Shaham, J., 1985, *ApJ*, 297, 16  
 Jaffe, W., 1983, *MNRAS*, 202, 995  
 King, I. R., 1996, *AJ*, 71, 65  
 Mihos, J. C., Hernquist L., 1994, *ApJ*, 437, L47  
 Moutarde, F., Alimi, J.-M, Bouchet, F. R., Pellat, R., 1995, *ApJ*, 441, 10  
 Navarro, J. F., White, S. D., 1993, *MNRAS*, 265, 271  
 Navarro, J. F., Frenk, C., White , S. D. M., 1995, *MNRAS*, 275, 56  
 Navarro, J. F., Frenk, C., White , S. D. M., 1995, *MNRAS*, 275, 720 (NFW)  
 Navarro, J. F., Frenk, C., White , S. D. M., 1996a, *ApJ*, 462, 563  
 Navarro, J. F., Frenk, C., White , S. D. M., 1996b, *ApJ*, in press.  
 Navarro J. F., Steinmetz M., 1996, *ApJ*, 438, 13  
 Persic M., Salucci P., Stel F., 1996, *MNRAS*, 281, 27 (PSS)  
 Quinn, P. J., Salmon, J. K., Zurek, W. H., 1986, *Nature*, 322, 329  
 Steinmetz, M., White, S. D. M., 1997, *MNRAS*, 289, 545  
 Teyssier, R., Chieze, J., Alimi, J.-M, 1997, *ApJ*, 480, 36  
 Thomas, P. A., Couchman, H. M. P., 1992, *MNRAS*, 257, 11  
 Tissera, P. B., Lambas, D. G., Abadi M., G., 1997, *MNRAS*, 286, 384  
 Tissera, P. B., Domínguez-Tenreiro, R. , Goldschmidt, P. , 1996, *Starburst Activity in Galaxies*, Ed. J. Franco, R. Terlevich, A. Serrano, *RevMexAA (Conf Series)*, vol. 6, p 225  
 Tormen G., Bouchet F. R., White S. D. M., 1997, *MNRAS*, 286, 865  
 Warren, W. S., Quinn, P. J., Salmon, J. K., Zurek, W. H., 1992, *ApJ*, 399, 405  
 White, S. D. M., Frenk, C., 1991, *ApJ*, 379, 52  
 Zurek, W. H., Salmon, J. K., Quinn, P. J., 1988, *ApJ*, 330, 519

## TABLE CAPTIONS

Table I: Main parameters of simulations:  $N_{part}$  is the total number of particles simulated,  $\Omega_b$  is the baryonic density parameter,  $b$  is the bias parameter,  $\eta$  and  $\rho_{star}$  ( $\text{gr}/\text{cm}^3$ ) are parameters of the star formation algorithm (see text for details).

Table II: Main parameters of halos in the AP3M (sets I.1, II.1) and SPH (sets I.2, I.3, II.2) runs:  $N_{dark}$ ,  $N_{star}$  and  $N_{gas}$  are the dark matter, star and gas numbers of particles, respectively, within the virial radius used to resolved the halos.  $M_{200}$  is the virial mass in units of  $10^{12}M_{\odot}$ ,  $r_{200}$  is the virial radius (kpc) and  $r_{cross}$  the crossing radius as defined in section 3.5 (kpc).  $c_{NFW}$  and  $c_{TD}$  are the concentration parameters for the fits of NFW profile and equation 6, respectively. GLO gives a general description of the shape of the main baryonic object in the halo: spheroidal (S), disk (D) (P denotes a pair of galactic-like objects).

**FIGURE CAPTIONS:**

Figure 1: Distribution of axis ratios  $b/a$  and  $c/a$  for halos in the purely dynamical (solid triangles) and hydrodynamical (open pentagons) simulations measured at the virial radius.

Figure 2: a) Semiaxes  $b/a$  (open) and  $c/a$  (solid) for 10 ellipsoids containing from 10% to 100% of the dark mass within  $r = 100$  kpc of halo 1 (triangles) and for halo 3 (pentagons) in simulation I.2; b) semiaxes  $b/a$  (open) and  $c/a$  (solid) for a halo in simulation I.2 (triangles) and I.3 (pentagons). The values at the virial radii have also been plotted.

Figure 3: a)  $\beta_{dark}$  as function of the radius for two halos in the SPH (heavy lines) and N-body (light lines) runs superposed; b) total velocity dispersion  $\sigma$  for 4 objects in simulation I.2 (heavy lines) and for their corresponding counterparts in simulation I.1 (light lines).

Figure 4: Dark matter density profiles for 4 halos in the purely dynamical simulation (I.1, solid line) and the best-fit given by NFW profile (dotted line). The arrow shows the gravitational softening.

Figure 5: Dark matter density profiles for 2 halos in simulation I.1 (dotted lines) and their counterparts in simulation I.2 (solid lines). The arrow shows the gravitational softening.

Figure 6: Dark matter density profiles for four halos in the hydrodynamical run I.2 (solid line), the best-fits given by NFW profile (dot-long dashed lines) and by equation 6 (dotted line). The arrow shows the gravitational softening.

Figure 7: The logarithm of the concentration parameters  $c_{NFW}$  for halos in I.1 (open pentagons), and  $c_{TD}$  for halos in I.2 (solid squares) and I.3 (open triangles). The curve is the predicted concentration from the collapse time of the halos in purely dynamical models using NFW profiles. The zero point of the relation for I.2 and I.3 has been redefined to match the value for I.1 in order to be able to compare the slopes.

Figure 8: The ratio of the dark matter masses within  $r = 30$  kpc for halos in the hydrodynamical ( $M_{dark}^{sph}$ ) simulations to their counterparts in purely gravitational ( $M_{dark}^{dyn}$ ) runs, versus their virial mass  $M_{200}$ , for halos in simulations I.2 (solid squares), I.3 (open triangles) and II.2 (open circles).

Figure 9: Density profiles of Halo 1 and Halo 4 in simulations I.2 and I.3: dark matter density profiles (solid lines) and baryonic density profiles in I.2 (dotted lines) and I.3 (dot-long dashed lines).

Figure 10: Circular velocity curves of the dark matter component for three halos in simulation I.2. We also include the analytical fit given by Eq.(8) (solid line). The arrows indicate twice the softening length used.

Figure 11 : Rotational velocity distributions for the baryonic particles of objects in simulation I.2 (solid triangles), circular velocity curves (according to equation 9) for the total mass distribution (solid line), the dark matter only (dot-dashed line) and the baryonic component (dotted line).

Figure 12: Circular velocity curves for objects in simulation I.3 for the total mass distribution (solid line), the dark matter only (dot-dashed line) and the baryonic component (dotted line).

Figure 13: a) The virial circular velocity ( $V_{200}$ ) and, b) the maximum of the circular velocity curve ( $V_{cir}^{max}$ ) versus the crossing radius ( $r_{cross}$ ) in units of the virial radius ( $r_{200}$ ), for halos in simulation I.2 (solid squares) and simulation I.3 (open triangles)

Figure 14: The ratio of the baryonic mass inside  $r_{cross}$  to the total baryonic mass at  $r_{200}$ , versus the total virial mass, for halos in simulations I.2 (solid squares), I.3 (open triangles) and II.2 (open circles). We have omitted Halo 7 in set I since it hosts a pair of disk-like objects.

Figure 15: Rotational velocity for baryonic particles in four disk-like objects in I.2 (solid triangles) and the best fit given by the URC proposed by Persic et al. (1996) (solid line).